Journal of Materials Chemistry C

ROYAL SOCIETY OF CHEMISTRY

PAPER

View Article Online
View Journal | View Issue

Cite this: J. Mater. Chem. C, 2025, 13, 19017

$AgGaS_2/Ga_2S_3$ quantum dots exhibiting efficient narrow blue emission

Avijit Saha, †*[ab] Siddhant Basel, †[a] Céline Rivaux,[a] Dmitry Aldakov[a] and Peter Reiss *[a]

Received 26th April 2025,
Accepted 9th August 2025

DOI: 10.1039/d5tc01686j

rsc.li/materials-c

Ternary metal chalcogenide quantum dots (QDs) have become an important class of materials characterised by a large tunability of the band gap and hence spectral range of light absorption and emission by changing their composition and size. They are an appealing alternative to toxic Cd-based NCs and offer a simpler synthetic process compared to III–V QDs such as InP or InAs. However, in the blue region, they typically exhibit broad emission peaks and low photoluminescence quantum yield (PLQY). Herein, we report $AgGaS_2/Ga_2S_3$ core–shell QDs emitting in the deep-blue region at 442 nm, and exhibiting a narrow line width (FWHM = 24 nm) as well as a PLQY exceeding 50% on passivation of defect states through treatment with tributylphosphine.

Introduction

Chemical engineering of heterostructure colloidal QDs has given rise to an unprecedented class of emissive materials for optoelectronic applications like photovoltaics, display and solid-state lighting.[1] Although Cd- and Pb-based materials have been widely investigated and demonstrated efficient device performance,[1] intrinsic toxicity of these heavy metals restricts their widespread use.[2] In search of environmentally friendly materials, InP-based QDs and their core–shell structures emerged as a potential replacement for cadmium-containing QD emitters.[3] Although InP-based QDs show excellent performance in the green[3,4] and red[5] regions, it is highly challenging to access the blue range of 440–460 nm.[6] The latter is technologically of utmost importance, in particular for the production of blue QD light-emitting diodes (QLEDs), which are required to realise electroluminescent pixels for next generation display technologies showing enhanced performance and reduced power consumption. Recently, Rakshit *et al.* and Roy *et al.* reported deep-blue (430 nm, PLQY 45%) and blue (462 nm, PLQY 50%) emission by synthesizing ultrasmall sized InP QDs with a ZnS shell, albeit with a comparably broad linewidth exceeding 70 nm.[7,8] So far $ZnSe_{1-x}Te_x$-based QDs performed best in blue QLEDs,[9–12] however, the high tendency for aggregation of tellurium atoms within the alloy structure can lead to spectral broadening and structural instability.[12] Moreover, the presence of tellurium raised concerns due to the toxicity of its oxyanions.[13] In the quest for novel blue emitters, we recently reported the synthesis of strongly emissive Ga_2S_3 nanocrystals, which exhibited a fast emission rate with a photoluminescence (PL) lifetime of around 1 ns in the deep blue range (400 nm).[14] However, the wavelength could not be tuned to longer wavelengths due to the wide band gap of the material.

Chalcopyrite-type I–III–VI_2 QDs emerged in the past 15 years as an alternative class of QD materials providing combined composition- and size-tuneable optical and electronic properties and opening up a novel space of compounds beyond well-established binary semiconductors.[15] In particular $CuInS_2$ and $AgInS_2$ QDs have been studied most widely due to their efficient luminescence and possibility to synthesise them both in organic medium or in the aqueous phase.[16–20] Although the PLQY of these QDs exceeds 50%, their broad PL line width due to an emission mechanism involving intra-bandgap trap states has been recognised as the major issue impeding their utilization in display applications, as these require narrowband emission to achieve a wide colour gamut.[21]

Recently, there have been several reports on I–III–VI_2-based QDs exhibiting narrow linewidth emission by the passivation of surface-related defect states using amorphous InS_x or GaS_x shells.[16,22–24] This approach enabled almost quantitative switching from defect-state-related to band-edge emission in contrast to widely applied ZnS shelling. The latter generally leads to partial alloying with the core and the generation of novel trap states. Nonetheless, the reported examples are focusing on materials emitting in the green to red region, most of them on $AgInS_2$-based QDs. Changing the trivalent metal from In^{3+} to Ga^{3+} gives access to larger bandgap energies and hence allows for blue-shifting the emission peak (E_g $AgInS_2$: 1.87 eV; $AgGaS_2$: 2.51 eV). While a couple of recent works

[a] Univ. Grenoble Alpes, CEA Grenoble, CNRS, Grenoble INP, IRIG, SyMMES, STEP, 38000 Grenoble, France. E-mail: avijitsaha@iitbhilai.ac.in, peter.reiss@cea.fr
[b] Department of Physics, IIT Bhilai, Durg, Chhattisgarh 491002, India
† These authors contributed equally to this work.

describe the synthesis of $AgGaS_2$ nanocrystals,[17,25–28] achieving narrow blue emission with high photoluminescence quantum yield (PLQY) remains a challenge. Herein, we report the synthesis of $AgGaS_2/Ga_2S_3$ (AGS–GS) core–shell QDs which exhibit strongly decreased defect state emission and narrow band-edge emission in the blue range at 442 nm (FWHM: 24 nm). (N.B.: for simplicity, $AgGaS_2/Ga_2S_3$ will be used independently of the precise composition determined *via* elemental analysis.) Surface passivation of these core–shell QDs using $GaCl_3$ and tributylphosphine (TBP) leads to a PLQY of 50%.

Experimental methods

Materials

Gallium(III) acetylacetonate ($Ga(acac)_3$, 99.99%), silver iodide, elemental sulphur (S, 99.99%), oleylamine (OLAm (90%)), gallium chloride (99.99%), aniline (99.5%), phenyl isothiocyanate (98%), tributylphosphine (TBP, 98%) were purchased from Sigma Aldrich.

Synthesis of *N*,*N*-diphenylthiourea (DPTU)

We used the procedure of Owen and coworkers to synthesise *N*,*N*-diphenylthiourea.[29] In a typical synthesis, 0.0369 mol (5 g) of phenyl isothiocyanate and 0.0186 mol of aniline were separately dissolved in 6 mL toluene in two flasks. The aniline solution was slowly added to the phenyl isothiocyanate solution while stirring. The obtained mixture was then stirred for 30 min at room temperature. The resulting white crystals were filtered off and washed with excess toluene. The product was dried under vacuum to obtain *N*,*N*-diphenyl thiourea as a white powder (yield 77%). ^{1}H-NMR (C_6D_6, 400 MHz): δ = 6.98 ppm (m, 10 H), 7.63 ppm (s, 2H).

Synthesis of $AgGaS_2$ QDs

$AgGaS_2$ core QDs were synthesised following the literature procedure with slight modifications.[17] In a typical synthesis, 0.5 mmol of $Ga(acac)_3$, 0.0625 mmol of AgI, and 5 mL OLAm were loaded in a 50 mL three-necked round-bottom flask equipped with a temperature controller probe and connected to a Schlenk line. This reaction mixture was degassed under vacuum for 30 min at 100 °C under constant stirring. 1.5 mL of 1-dodecanethiol (DDT) was injected into the mixture and degassed further for 10 min. The flask environment was switched to argon, and the temperature was raised to 150 °C. 1 mmol of sulphur, dissolved at 40 °C in 2 mL of OLA, was injected into the reaction mixture. The temperature was then raised to 240 °C and maintained for 30 min. The reaction was then cooled down to room temperature by removing the reaction flask from the heating mantle and putting it into a water bath. The $AgGaS_2$ nanocrystals were separated from the reaction medium by precipitation with anhydrous ethanol, centrifugation and redispersion in 1 mL of hexane and stored for the next step of core–shell synthesis.

Synthesis of $AgGaS_2/Ga_2S_3$ core–shell QDs

In a typical synthesis, 350 µl of the above-prepared $AgGaS_2$ core QD solution were mixed with 0.15 mmol (60 mg) of $Ga(acac)_3$, 0.15 mmol (34 mg) of DPTU and 8 mL of OLAm in a three-necked flask equipped with a temperature control probe and condenser and connected to a Schlenk line. The reaction mixture was degassed and the temperature was increased slowly to 90 °C while degassing and then maintained for 30 min to fully remove hexane. Subsequently, the flow was switched to Ar, and the solution temperature was increased rapidly to 230 °C and afterwards slowly to 280 °C at a rate 2 °C min^{-1} for the Ga_2S_3 shell growth. In a separate vial, 0.3 mmol (70 mg) of gallium chloride was dissolved in 2 mL of OLAm inside a glove box. When the temperature of the reaction flask reached 280 °C, the $GaCl_3$ solution was slowly injected into the reaction mixture and the temperature was maintained for further 75 min. Finally, the core–shell samples were washed thrice by precipitation using a hexane/ethanol mixture, centrifugation and redispersion of the precipitate in 5 mL of hexane. For TBP treatment, the core–shell QDs in hexane were taken inside a glove box and 50–100 µL of TBP were added and mixed by stirring for 30–60 min.

Characterization

The UV-VIS absorption spectra of the samples were recorded using a Hewlett Packard 8452A spectrometer. The steady-state and time-resolved PL spectra were obtained using a Horiba Fluorolog FL1057 spectrophotometer equipped for the measurement of the absolute PLQY with an integrating sphere. For time-resolved PL measurements, the same instrument was used and a pulsed laser diode (360 nm) for the excitation; the curves were fitted as described in the SI. Temperature-dependent PL spectra were recorded on an Edinburgh Instruments FS5 spectrometer using an Oxford Instruments Optistat DN cryostat cooled with liquid nitrogen and equipped with a Mercury ITC controlling unit. X-ray diffraction patterns for the nanocrystal QDs were recorded on a Bruker diffractometer using Cu-Ka (l = 1.5406 Å) radiation. Transmission electron microscopy was performed on an FEI TECNAI microscope operating at 200 kV and the images were recorded on a Gatan K2 camera. Chemical characterization by XPS was carried out using a Versaprobe II ULVAC-PHI spectrometer. All XPS measurements were carried out in an ultra-high vacuum chamber (7×10^{-8} mbar). The samples for XPS were prepared on silicon substrates by spin-coating the QDs and washed with ethanol to remove the extra ligands. Curve fitting and background subtraction were accomplished using Casa XPS 2.3 software. Binding energies are referenced with respect to adventitious carbon (C 1s BE = 284.8 eV). Inductively coupled plasma optical emission spectroscopy (ICP-OES) measurements were performed on a Shimadzu 9000 spectrometer. The samples were prepared by dissolving the precipitated QDs in Millipore water with 10% HNO_3. Standard solutions of the metal ions were prepared by diluting ICP standards of Ag and Ga with HNO_3 10% (v/v).

Results and discussion

Optical properties of the QDs

$AgGaS_2$ (AGS) QDs were synthesised in a hot-injection approach based on the heat-up method reported in ref. 17 at 240 °C using

gallium acetylacetonate, silver iodide, and elemental sulphur/dodecanethiol as the metal and sulphur sources, respectively, and oleylamine as the solvent (*cf.* Fig. 1(a)). Fig. 1(b) shows the UV-VIS absorption and photoluminescence (PL) spectra of the AGS QDs. While the absorption spectrum is featureless as in the overwhelming majority of ternary chalcogenide QDs, the PL spectrum shows a small, narrow peak at 442 nm and a broad peak centred at around 520 nm, tentatively attributed to band-edge and trap state-assisted emission.[17] It should be specified that only when using good vacuum conditions during the degassing step (around 5×10^{-2} mbar), the small peak at 442 nm is visible in the final sample. The inset of Fig. 1(b) illustrates the Tauc plot obtained from the absorption spectrum used to determine the optical band gap of the AGS QDs of 2.89 eV. For the growth of the gallium sulphide (GS) shell, the same gallium precursor was applied whereas diphenylthiourea was selected as the sulphur precursor (*cf.* Fig. 1(a)). Substituted thioureas have been proven to be very versatile precursors in the synthesis of PbS QDs, as they can be easily synthesised and their reactivity readily tuned by changing the substituents.[30]

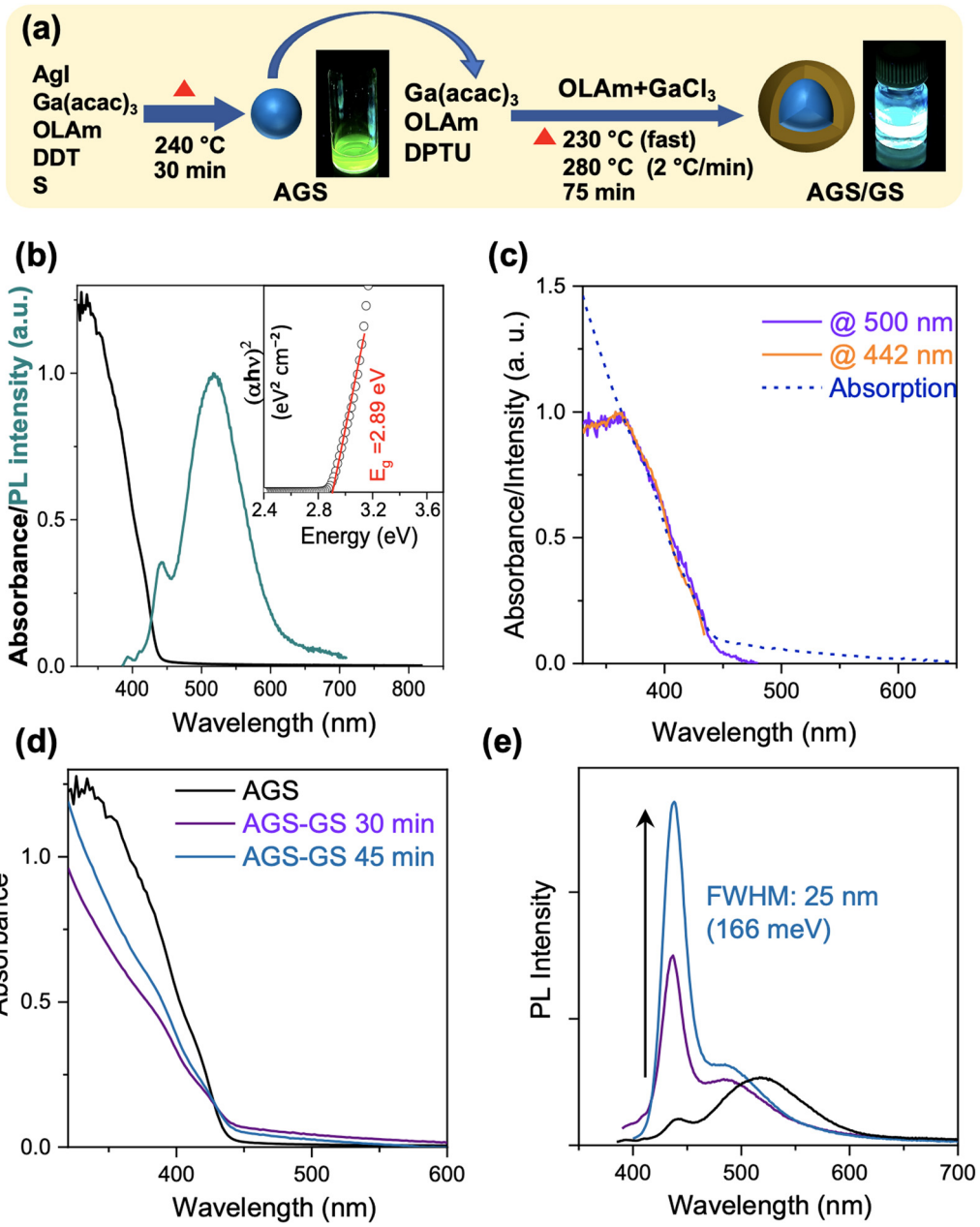

Fig. 1 (a) Schematic representation of the synthesis method for AGS core and AGS–GS core–shell QDs. (b) UV-VIS absorption (black) and PL spectra (dark cyan) of AGS core QDs. The inset shows the Tauc plot used to determine the optical band gap. (c) PLE scan of AGS–GS core–shell QDs (30 min reaction time) measured at the 442 and 500 nm emission peaks in comparison with the absorption spectrum (dashed line). (d) Absorption spectra of AGS core and AGS–GS core–shell QDs obtained with reaction times of 30 min and 45 min. (e) PL spectra of the same samples, normalised for absorbance at the excitation wavelength of 350 nm.

While the core AGS QDs show green emission, AGS–GS core–shell QDs exhibit blue emission under UV light exposure. Fig. 1(d) and (e) show the comparison of the UV-VIS absorption and PL spectra of AGS core and AGS–GS core–shell QDs obtained with different times of shell growth. With the growth of the Ga_2S_3 shell, the broadband trap-state emission of the AGS core QDs is successively suppressed, while the shorter wavelength band-edge peak was enhanced resulting in an intense and sharp blue emission at 442 nm (full width at half maximum, FWHM = 25 nm). This behaviour is attributed to the efficient surface passivation of the AGS core with the larger band gap Ga_2S_3 shell. To further study the origin of the sub-band-gap and band-gap transitions, we recorded the PL excitation (PLE) spectra. Fig. 1(c) shows the PLE scans of the AGS–GS sample obtained after 30 min, collected for the PL emissions at 442 and 500 nm, respectively. Both PL excitation spectra are very similar to the absorption spectrum suggesting that, while the emission occurs through both defect states and band edges, light absorption is dominated by the host semiconductor's bandgap.

To get more insight into the nature of the PL emission, we recorded time-resolved photoluminescence (TRPL) spectra at 442 and 520 nm (Fig. 2(a) and (b)). The TRPL data are summarised in Table 1. The decay curves were fitted using tri-exponential functions resulting for the AGS core QDs in an average lifetime of 45 ns at 442 nm and 118 ns at 520 nm. The significantly longer lifetime of the broad peak suggests trap-assisted emission involving mid-gap states. On the other hand, the relatively short lifetime with the peak position 2.82 eV, similar to the bandgap determined from the absorption spectrum, support the assumption that the 442 nm peak is related to band-edge emission.[18]

Noteworthy, the average lifetimes of both the band-edge and mid-gap-related emissions decreased from AGS to AGS–GS QDs due to the suppression of surface defect states. The lifetime value of the mid-gap peak of the gallium sulphide capped AGS–GS QDs is much smaller than that reported by Guo and coworkers for zinc sulphide capped AGS–ZnS QDs[26] where a value of 1723 ns was obtained, demonstrating the passivation mechanism is completely different.

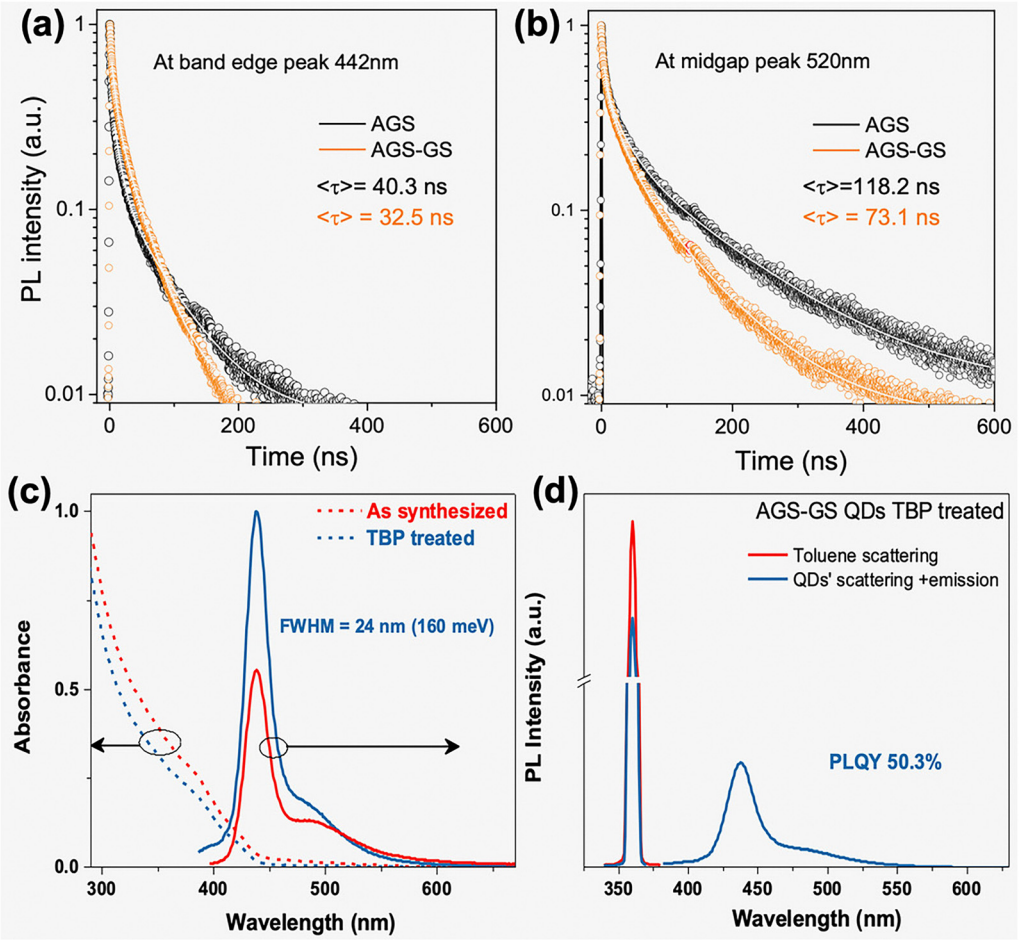

Fig. 2 PL decay curves measured at (a) 442 nm and (b) 500 nm for the AGS core and AGS–GS core–shell QDs fitted with tri-exponential functions (solid lines). (c) UV-vis and PL spectra of the AGS–GS core–shell QDs before and after TBP treatment. (d) Absolute PLQY measurement of the TBP-treated AGS–GS QDs using an integrating sphere.

Table 1 TRPL data of the AGS core and AGS–GS core–shell QDs

Sample	λ_{Em} (nm)	τ_1 (ns)	A_1	τ_2 (ns)	A_2	τ_3 (ns)	A_3	$\langle\tau\rangle$ (ns)
AGS core	442	1.8	56.5	10.9	30.0	63.4	13.5	45.0
AGS–GS	442	2.5	41.0	14.4	38	48.9	21.0	34.8
AGS core	520	4.5	50.3	29.4	30	152.1	19.7	118.2
AGS–GS	520	3.7	46.7	25.1	33.3	99.4	20.0	73.1

In contrast, Tang and coworkers determined an average lifetime of 67.1 ns for Ag–Ga–Zn–S (AGZS) QDs, *i.e.*, close to our values, however, the average lifetime is reduced due to a fast non-radiative component giving rise to comparably low PLQYs of 2% (AGS) and 16.7% (AGZS). Also the linewidth is with 48 nm FWHM considerably broader, which may be a sign of the contribution of intragap states related to zinc doping.[27]

To achieve a better surface passivation, we treated the QDs with tributylphosphine (TBP), which has been shown to improve the PLQY and reduce the defect emission in the case of $AgInS_2/GaS_x$ QDs.[16,22,31] TBP acts as an L-type ligand, coordinating with Ga^{3+} ions on the QD surface. This coordination effectively passivates dangling bonds associated with surface Ga^{3+} ions, thereby reducing the density of trap states. Additionally, TBP facilitates the removal of surface sulphur sites through conversion to the more stable tributylphosphine sulphide. After the surface treatment, the intensity of the band edge emission enhanced dramatically (Fig. 2(c)). As a result, we observe a narrow band (FWHM 24 nm) intense blue emission with a PLQY of 50.3 ± 2.5% (Fig. 2(d)), while the untreated sample exhibits a value of 34% with a more pronounced contribution of trap-state emission. The TBP treatment did not induce any significant change in the absorption spectra (Fig. S1a). Furthermore, the transition energies determined from the second derivative of the absorption spectra remained unchanged, indicating that the size of the AGS–GS core–shell QDs was not affected by the treatment (Fig. S1b).[32] An increase in the average PL lifetime following TBP treatment suggests effective passivation of surface defects (Fig. S2 and Table S1). Notably, the first, fast component of the triexponential fit – commonly associated with nonradiative recombination *via* surface defects – was substantially reduced after treatment. Prior to the TBP treatment, this component accounted for 8% of the decay, which decreased to 2.6% post-treatment. Taken together with the simultaneous enhancement of the PLQY confirms that the TBP treatment leads to the decrease of nonradiative recombination *via* surface defects.[33] FTIR studies indicate that the native ligands of the AGS–GS core–shell QDs remain on the surface after the TBP treatment, likely with the additional presence of TBP, as revealed by the comparison of FTIR spectra recorded before and after the treatment showing the appearance of the P–C stretching band at 1154 cm^{-1} (Fig. S3).

The emission peak position, PLQY, and FWHM of previously reported I–III–VI based QDs emitting in a similar region and/or applying gallium sulphide shelling are summarized in Table 2. These QDs show efficient emission in the longer wavelength range (green or yellow) by incorporating In with Ga or purely using In. However, in the blue region either a low PLQY or a broad emission line width have been observed. This comparison highlights that the current AGS/GaS QDs represent a significant improvement and offer an effective combination of narrowband deep-blue emission with high PLQY.

Table 2 Reported PL-emission peak positions, PLQY and FWHM values of various I–III–VI based QDs in comparison with the current work

Composition	Emission peak position	PLQY (%)	FWHM (nm)
AGS@GaS QDs[34]	446 nm (deep blue)	12	22
$Ag(In_xGa_{1-x})S_2/GaS$ QDs[22]	498 nm (green)	28	32–42
	556 nm (yellow)	59	
$Ag(In_xGa_{1-x})S_2/GaS$ QDs[35]	499 nm (green)	21	31–37
	543 nm (yellow-green)	75	
AGS/ZnS QDs[25]	482 nm (blue)	21	90
ZnAGS/ZnS[17]	450 (blue)	58–60	>130
$AgInS_2/GaS$[16]	~580 nm (yellow)	56	24
AGS/GaS QDs (current work)	**442 nm (deep blue)**	**50**	**24**

We now turn to the structural characterization of the AGS and AGS–GS QDs. Bright-field TEM and HRTEM images of the core and core–shell QDs along with their size distribution analysis are shown in Fig. 3. AGS core QDs have nearly spherical morphology with an average size of 3.74 ± 0.48 nm. With the growth of the GaS_x shell, the average particle size increased to 5.1 ± 0.62 nm, which corresponds to a shell thickness of around 0.7 nm. In HRTEM images, the lattice fringes are visible for both the core and core–shell QDs, however, the core and shell part in these QDs cannot be conclusively distinguished as there is no marked difference in the TEM contrast. Nonetheless, the lattice fringes, spaced by a distance of 0.326 nm, appear to extend throughout the whole particle size in the core–shell nanocrystals, indicating the crystalline nature of the shell. TEM analysis also demonstrates that the QDs maintain a

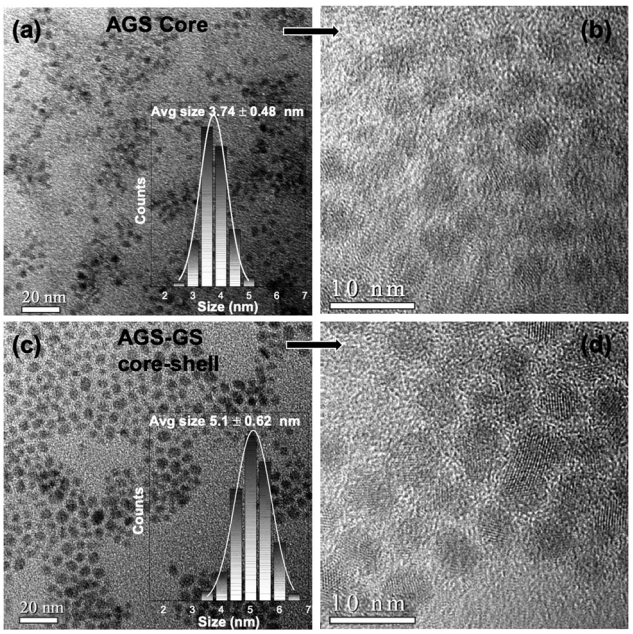

Fig. 3 TEM (a), (c) and HRTEM (b), (d) images of core AGS (a), (b) and core–shell AGS–GS QDs (c), (d), respectively. Insets of (a) and (b) show the corresponding size distributions and calculated average size.

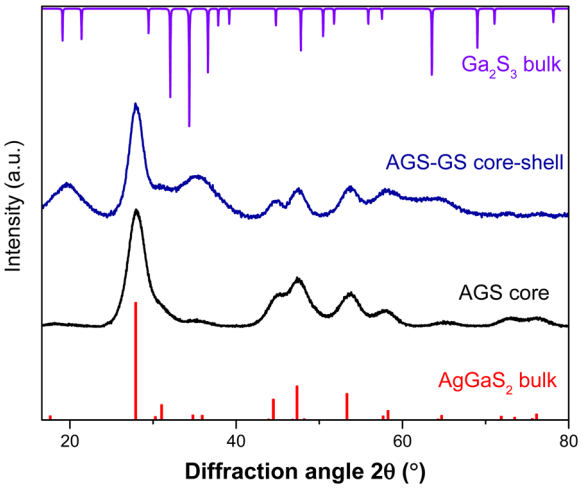

Fig. 4 XRD patterns of the AGS core and AGS–GS core–shell QDs in comparison with bulk $AgGaS_2$ in the tetragonal phase (ICSD 01-073-1233) and monoclinic Ga_2S_3 (ICSD 00-050-0811) diffraction patterns from ICSD database.

nearly spherical morphology showing a uniform increase in size with the GaS_x growth. The absence of any other separate size distribution, along with the unaltered morphology and uniform growth thus confirm the successful formation of the GaS_x shell on AGS core QDs. The powder X-ray diffraction (XRD) pattern of AGS matches well the pattern of bulk $AgGaS_2$ in the tetragonal phase (Fig. 4) with no other peaks related to impurities. After the overcoating with the shell, additional peaks are observed at positions matching those of monoclinic Ga_2S_3 corroborating the existence of the core–shell heterostructure with a crystalline shell.

Table 3 summarises the results of elemental analysis using inductively coupled plasma optical emission spectroscopy (ICP-OES). As expected from the size increase, the Ga : Ag ratio increases during the Ga_2S_3 shell growth from 1.5 (AGS) to 3.6 (AGS–GS). The S : Ag ration, in turn, shows a much smaller increase than expected. On the other hand, the precise determination of sulphur is generally not possible with ICP due to the formation of gaseous H_2S during the mineralisation of the QDs.

A more precise analysis of the sulphur content is possible using X-ray photoelectron spectroscopy (XPS). High-resolution XPS scans of the constituting elements (Ag, Ga, S) of the core and core–shell QDs are depicted in Fig. 5. The results from elemental analysis obtained from the ratios between the integrated intensity of the key elements can be found in Table 2. As for ICP-OES, XPS confirms that the Ga and S amount has significantly increased after shell growth. Noteworthy, the amount of S obtained from XPS is higher compared to ICP-OES due to the absence of the aforementioned issues with sulphur loss and additional contribution of DDT ligands. The size of the QDs including their organic ligand shell of more than 7 nm exceeds the escape depth of photoelectrons (typically 3–5 nm), which explains the lower Ga increase (factor 1.6) during shell growth observed with XPS than the value obtained with ICP (factor 2.4). Both techniques, however, consistently show that the AGS core QDs are Ag-deficient. This off-stoichiometry was intentional as we deliberately used a sub-stoichiometric Ag:Ga precursor ratio, motivated by previously reported I–III–VI nanocrystals in which the electronic structure, including the bandgap and the positions of the valence and conduction bands, could be effectively tuned through the metal ion composition.[25,36,37] It was observed from the semiconductor band structure that the group I (Ag) d-states and the group VI (S) p-states predominantly construct the valence band maxima.[37] The weaker p–d repulsion in the Ag-deficient AGS core lowers the valence band maximum and thereby increases the band gap. This effect was exploited here to achieve a wider bandgap, enabling deep-blue emission in the obtained AGS QDs. In addition to the band gap tuning, it was also consistently observed that group III-rich I–III–VI QDs show a higher PLQY than group I-rich compositions.[15,38,39] Thus, Ag-deficiency in the AGS core QDs was a beneficial choice in order to achieve a wider band gap, deep blue emission, and high PLQY. We note that the actual Ag : Ga ratio in the QDs deviates significantly from the precursor feed ratio (8 : 1 Ga : Ag). Therefore, we can conclude that the reactivity of both precursors differs markedly and even for very low silver-to-gallium ratios the AGS core synthesis, the reaction likely proceeds *via* the formation of Ag_2S seeds into which Ga is incorporated.[35] Also, this large discrepancy between the feed ratio and actual composition makes the precise control of the emission wavelength challenging.

The XPS signal of Ag $3d_{5/2}$ in the core QDs is observed at 367.9 eV in agreement with previous studies on $AgGaS_2$ nanocrystals due to the presence of Ag^+ (Fig. 5(a)).[28,40] For the Ga 3d energy region, a characteristic doublet is observed with peaks at 19.7 and 20.1 eV corresponding to Ga $3d_{5/2}$ and Ga $3d_{3/2}$, respectively. In addition, we clearly observe a Ga $2p_{3/2}$ peak at 1117.7 eV likely corresponding to Ga^{3+} species, in line with the expected AGS composition and oxidation states. In order to confirm the chemical nature of Ga, which is often elusive, we have also recorded the LMM peak and calculated its Auger parameter (BE(Ga $3d_{5/2}$ – KE(Ga $L_5M_{45}M_{45}$))) as 1084.3 eV. This parameter is close to the previously reported value for $AgGaS_2$ (1084.6 eV) and is considerably different from that of oxidised gallium in Ga_2O_3 (1082.9 eV) confirming that gallium is present in the synthesised core QDs in the expected Ag–Ga–S configuration without significant oxidation.[28,41] The S-core level spectrum can be deconvoluted into a doublet with an S $2p_{3/2}$ peak at 161.8 eV consistent with the expected S^{2-} in the sulphide form together with a contribution of Ga 3s. Noteworthy, no oxidised sulphur is observed at *ca.* 168 eV. For the core–shell QDs, similar spectra are observed corresponding to the Ag^+, Ga^{3+} signals (equally confirmed by the Auger parameter of 1084.4 eV) with the contributions of defect-related peaks and absence of

Table 3 Atomic ratios of AGS and AGS–GS QDs (normalised to Ag) from ICP-OES and XPS

Technique	Sample	Avg. size/nm (TEM)	Ag	Ga	S
ICP-OES	AGS core	3.74	1	1.5	1.6
	AGS–GS	5.1	1	3.6	2.1
XPS	AGS core	3.74	1	2.1	3.4
	AGS–GS	5.1	1	3.4	5.6

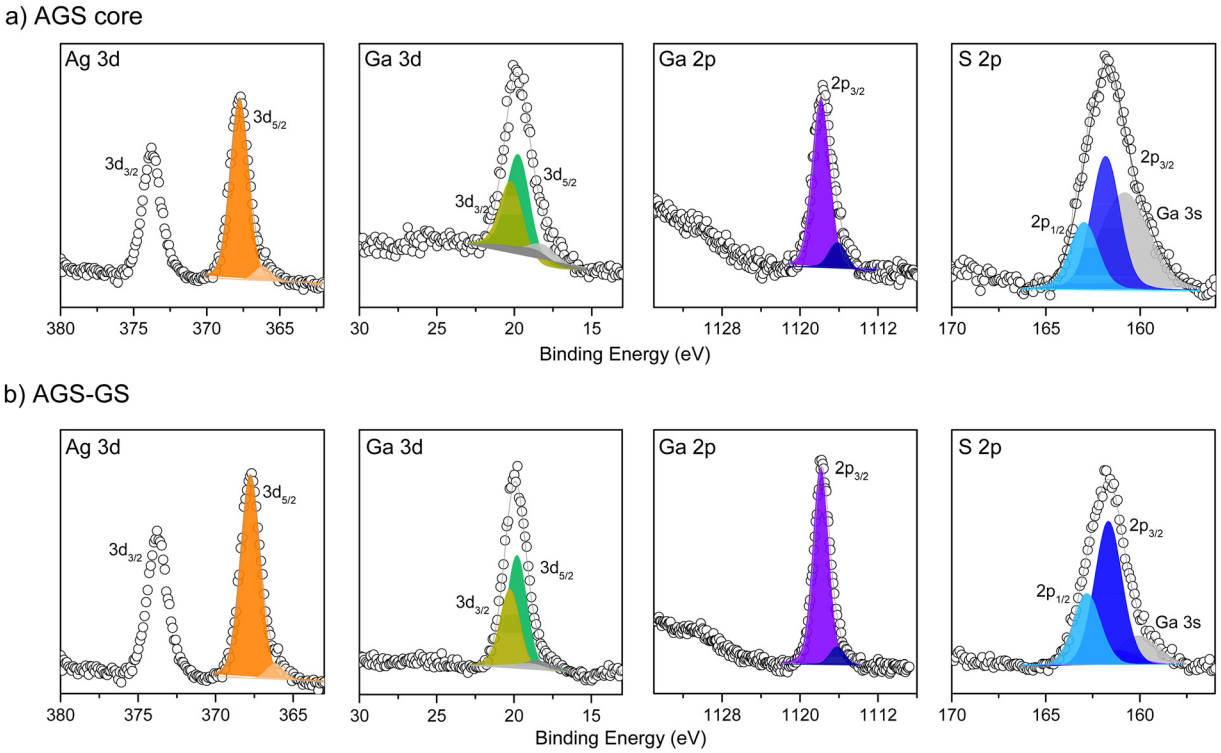

Fig. 5 High-resolution XPS spectra of Ag 3d, Ga 3d, Ga $2p_{3/2}$, and S 2p regions for (a) AGS core and (b) AGS–GS core–shell QDs. N.B.: the small peak visible at lower energies is related to the sample charging due to the presence of insulating organic ligands.

oxidation, as well as S^{2-} (Fig. 5(b)). These results, along with the XRD, TEM and optical properties, unambiguously confirm the formation of AGS core and AGS–GS core–shell quantum dots.

To further elucidate the mechanism behind the trap-state passivation upon shell formation, we performed temperature-dependent PL studies in a range of 78–298 K using a liquid nitrogen-cooled cryostat. The qualitative behaviour of the three samples studied – AGS core, AGS–GS core–shell, and TBP-treated AGS–GS QDs – is visible in Fig. 6.

The most striking difference between the core and core–shell samples is the fact that at temperatures below 200 K, the core QDs do not show two distinct emission peaks but only one broad feature, which exhibits high intensity for the lowest temperatures studied (78–108 K). On the contrary, the core–shell samples show the band-edge and trap-related peaks throughout the whole temperature range studied. For the TBP treated sample, the intensity of the 442 nm band edge peak is always higher than that of the trap-related one, while for the pristine AGS–GS QDs a crossover takes place at around 150 K. A more detailed analysis is provided in Fig. S4, which compares the 2D PL spectra, peak intensity, energy, and line width as a function of the temperature for the three samples. Considering the PL intensity (Fig. S4b, f and j), the two core–shell samples exhibit a sharp increase in the band edge emission at 200–230 K, which is almost 6-fold for AGS–GS and 3-fold for AGS–GS-TBP. This increase is much lower for the trap-state emission due to its different origin. While the intensity decrease on the longer wavelength side likely originates from the thermal activation of non-radiative recombination pathways,[42,43] the drop in intensity at temperatures below 200 K

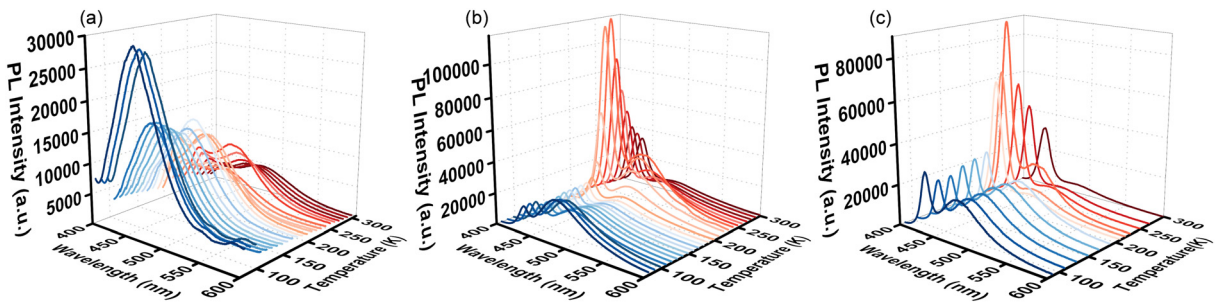

Fig. 6 Temperature-dependent PL spectra of AGS core (a), AGS–GS core–shell (b) and AGS–GS-TBP (c) QDs, using an excitation wavelength of 360 nm and hexane as the solvent (N.B.: the slit widths had to be reduced for the AGS–GS-TBP sample due to the higher intensity leading to saturation).

is unexpected. Antipov *et al.* had observed the increase of the PL intensity by a factor of approximately 1.5 of CdSe/ZnS QDs near the solvent phase transition, ice/water in that case, attributed to ligand reorganisation near the melting point of water.[44] In a recent work on Ag_2S nanocrystals, Meijerink and coworkers assigned the apparent PL intensity increase by a factor of 9–15 at around 210 K also to the solidification of the solvent (chloroform),[45] however, with a simpler argument not relying on the modification of the nanoparticle surface state: while in the liquid state the light can penetrate the whole sample volume, in the solid state only a surface layer is probed due to strong light scattering. To check whether this explanation applies to our samples, we kept the temperature for a longer time slightly above the melting point of hexane (190 K) where in the initial dataset no increase of the PL intensity could be observed yet due to short delay between the measurements, performed in 10 K steps. After 5 min delay between the two consecutive PL spectra at 208 K, the intensity of the band edge peak had increased by a factor of 2.3, confirming the abovementioned solvent phase transition as the origin of the PL decrease at low temperature. Therefore, the quantitative analysis of the temperature dependence of the PL intensity is challenging. Additional insight can be gained by analysing the PL decay at different temperatures (*cf.* Fig. S5 and Table S2). Comparing the data of AGS–GS QDs acquired at 78 K and 298 K revealed that the PL lifetime decreased by a factor of 3.4 for the trap-state emission compared to a factor of 2 for the band-edge peak. The pronounced shortening of the trap-state PL lifetime is indicative of the thermal activation of nonradiative decay channels. The evolution of the PL energy of the two core–shell samples also shows a discontinuity at around 200 K (*cf.* Fig. S4c, g and k): above this temperature we observe a steady decrease of the peak energy, as expected for the temperature-dependent evolution of the band gap induced by lattice expansion and exciton–phonon coupling.[45] Both the band-edge and the trap-state related emission peaks exhibit a similar temperature dependence, whereas the evolution of their line width markedly differs (Fig. S4d, h and l). While it globally increases with temperature, consistent with enhanced exciton–phonon coupling,[42] this increase is significantly more pronounced for the trap-state emission (approximately 90 meV) than for the band-edge peak (30 meV) in the two core–shell samples. The strong broadening of the former mainly occurs in the higher temperature range above 220 K, indicating in accordance with the above-discussed TRPL results, that additional trap-related recombination channels are thermally activated.

Conclusions

Summarizing, we present a synthetic method to produce blue-emitting QDs using non-toxic I–III–VI-based ternary semiconductors. While the $AgGaS_2$ core QDs show two PL peaks, the growth of a crystalline gallium sulphide shell suppresses to a large extent defect-induced mid-gap states resulting in enhanced band-edge emission at 442 nm with an absolute PLQY of 34%. The latter could be further enhanced to 50% by means of post-synthetic treatment with an organic L-type ligand (tributylphosphine), which demonstrates that complete passivation is not achieved with the gallium sulphide shell. The band-edge PL peak has a linewidth (FWHM) of 24 nm, which is similar to the best reported values in this wavelength region. The formation of the core–shell heterostructure was confirmed using XRD, TEM, ICP and XPS. Temperature-dependent PL studies reveal the existence of thermally activated nonradiative recombination channels leading to a pronounced line broadening of the trap-state emission in the 200–300 K range. To reach even better monochromaticity with fully suppressed trap-state emission as well as PLQY values competitive with the best QD systems, the surface passivation of AGS–GS nanocrystals needs to be further optimised, eventually *via* the identification of suitable outer shell materials.

Author contributions

Avijit Saha – investigation, writing – original draft, writing – review & editing; Siddhant Basel – investigation, writing – review & editing; Céline Rivaux – investigation; Dmitry Aldakov – investigation, writing – review & editing; Peter Reiss – funding acquisition – supervision – investigation – writing – review & editing.

Conflicts of interest

The authors have no conflicts of interest to declare.

Data availability

The data supporting this work are included in the article, raw data are available upon reasonable request from the authors.

TRPL analysis, FTIR data, temperature-dependent PL data, additional TRPL data. See DOI: https://doi.org/10.1039/d5tc01686j

Acknowledgements

The authors gratefully acknowledge financial support from Samsung (SAIT GRO grant EQUINOX) and from the French National Research Agency (grants ANR 18-CE09-0039-01 FLUO and ANR-24-CE09-0786-01 PIQUANT). The authors thank Stéphanie Pouget for assistance with powder X-ray diffraction.

References

1 Y. Deng, F. Peng, Y. Lu, X. Zhu, W. Jin, J. Qiu, J. Dong, Y. Hao, D. Di, Y. Gao, T. Sun, M. Zhang, F. Liu, L. Wang, L. Ying, F. Huang and Y. Jin, *Nat. Photonics*, 2022, **16**, 505–511.
2 P. Reiss, M. Carrière, C. Lincheneau, L. Vaure and S. Tamang, *Chem. Rev.*, 2016, **116**, 10731–10819.
3 P. Yu, S. Cao, Y. Shan, Y. Bi, Y. Hu, R. Zeng, B. Zou, Y. Wang and J. Zhao, *Light: Sci. Appl.*, 2022, **11**, 162.
4 W.-C. Chao, T.-H. Chiang, Y.-C. Liu, Z.-X. Huang, C.-C. Liao, C.-H. Chu, C.-H. Wang, H.-W. Tseng, W.-Y. Hung and P.-T. Chou, *Commun. Mater.*, 2021, **2**, 96.

5 Y.-H. Won, O. Cho, T. Kim, D.-Y. Chung, T. Kim, H. Chung, H. Jang, J. Lee, D. Kim and E. Jang, *Nature*, 2019, **575**, 634–638.
6 K. D. Wegner, S. Pouget, W. L. Ling, M. Carrière and P. Reiss, *Chem. Commun.*, 2019, **55**, 1663–1666.
7 S. Rakshit, B. Cohen, M. Gutiérrez, A. A. O. El-Ballouli and A. Douhal, *ACS Appl. Mater. Interfaces*, 2023, **15**, 3099–3111.
8 P. Roy, M. Virmani and P. P. Pillai, *Chem. Sci.*, 2023, **14**, 5167–5176.
9 S. Liang, Z. Tang, S. Li, X. Guo, S. Jia and X. W. Sun, *Adv. Opt. Mater.*, 2025, **13**, 2500034.
10 Z. Huang, H. Shen, Y. Wu, Y. Wu, W. Xu, X. Zhang and Y. Wang, *Appl. Phys. Rev.*, 2024, **11**, 021419.
11 Z. Huang, Q. Sun, S. Wang, H. Shen, W. Cai and Y. Wang, *Nano Lett.*, 2023, **23**, 4032–4038.
12 M. Imran, W. Paritmongkol, H. A. Mills, Y. Hassan, T. Zhu, Y.-K. Wang, Y. Liu, H. Wan, S. M. Park, E. Jung, J. Tam, Q. Lyu, G. F. Cotella, P. Ijaz, P. Chun and S. Hoogland, *Adv. Mater.*, 2023, **35**, 2303528.
13 T. G. Chasteen, D. E. Fuentes, J. C. Tantaleán and C. C. Vásquez, *FEMS Microbiol. Rev.*, 2009, **33**, 820–832.
14 A. Saha, R. Yadav, D. Aldakov and P. Reiss, *Angew. Chem., Int. Ed.*, 2023, **62**, e202311317.
15 D. Moodelly, P. Kowalik, P. Bujak, A. Pron and P. Reiss, *J. Mater. Chem. C*, 2019, **7**, 11665–11709.
16 T. Uematsu, K. Wajima, D. K. Sharma, S. Hirata, T. Yamamoto, T. Kameyama, M. Vacha, T. Torimoto and S. Kuwabata, *NPG Asia Mater.*, 2018, **10**, 713–726.
17 J.-H. Kim, B.-Y. Kim, E.-P. Jang, S.-Y. Yoon, K.-H. Kim, Y. R. Do and H. Yang, *J. Chem. Eng.*, 2018, **347**, 791–797.
18 A. Raevskaya, V. Lesnyak, D. Haubold, V. Dzhagan, O. Stroyuk, N. Gaponik, D. R. T. Zahn and A. Eychmüller, *J. Phys. Chem. C*, 2017, **121**, 9032–9042.
19 A. Delices, D. Moodelly, C. Hurot, Y. Hou, W. L. Ling, C. Saint-Pierre, D. Gasparutto, G. Nogues, P. Reiss and K. Kheng, *ACS Appl. Mater. Interfaces*, 2020, **12**, 44026–44038.
20 C. Rivaux, T. Akdas, R. Yadav, O. El-Dahshan, D. Moodelly, W. L. Ling, D. Aldakov and P. Reiss, *J. Phys. Chem. C*, 2022, **126**, 20524–20534.
21 J. Fan, C. Han, G. Yang, B. Song, R. Xu, C. Xiang, T. Zhang and L. Qian, *Adv. Mater.*, 2024, **36**, 2312948.
22 W. Hoisang, T. Uematsu, T. Torimoto and S. Kuwabata, *Inorg. Chem.*, 2021, **60**, 13101–13109.
23 G. Motomura, K. Ogura, Y. Iwasaki, T. Uematsu, S. Kuwabata, T. Kameyama, T. Torimoto and T. Tsuzuki, *Appl. Phys. Lett.*, 2020, **117**, 091101.
24 T. Torimoto, T. Kameyama, T. Uematsu and S. Kuwabata, *J. Photochem. Photobiol., C*, 2023, **54**, 100569.
25 T. Bai, X. Wang, Y. Dong, S. Xing, Z. Shi and S. Feng, *Inorg. Chem.*, 2020, **59**, 5975–5982.
26 H. X. Lu, H. Liu, Z. Z. Fu, Y. Y. Chen, H. Q. Dai, Z. Hu, W. L. Zhang and R. Q. Guo, *J. Mater. Sci. Technol.*, 2024, **169**, 235–242.
27 X. Xie, J. Zhao, O. Lin, Z. Yin, X. Li, Y. Zhang and A. Tang, *J. Phys. Chem. Lett.*, 2022, **13**, 11857–11863.
28 Y. Azhniuk, B. Lopushanska, O. Selyshchev, Y. Havryliuk, A. Pogodin, O. Kokhan, A. Ehm, V. Lopushansky, I. Studenyak and D. R. T. Zahn, *Phys. Status Solidi B*, 2022, **259**, 2100349.
29 M. P. Hendricks, M. P. Campos, G. T. Cleveland, I. Jen-La Plante and J. S. Owen, *Science*, 2015, **348**, 1226–1230.
30 P. Machut, A. K. Antonini, C. Rivaux, M. Gromova, H. Kaur, W. L. Ling, G. Mugny and P. Reiss, *Nano Res.*, 2024, **17**, 10677–10684.
31 W. Hoisang, T. Uematsu, T. Torimoto and S. Kuwabata, *Nanoscale Adv.*, 2022, **4**, 849–857.
32 A. Hirase, Y. Hamanaka and T. Kuzuya, *J. Phys. Chem. Lett.*, 2020, **11**, 3969–3974.
33 X. Xie, J. Zhao, O. Lin, Z. Yin, X. Li, Y. Zhang and A. Tang, *J. Phys. Chem. Lett.*, 2022, **13**, 11857–11863.
34 M. Tozawa, S. Ofuji, M. Tanaka, K. Akiyoshi, T. Kameyama, T. Yamamoto, G. Motomura, Y. Fujisaki, T. Uematsu, S. Kuwabata and T. Torimoto, *ACS Appl. Mater. Interfaces*, 2024, **16**, 68169–68180.
35 T. Uematsu, M. Tepakidareekul, T. Hirano, T. Torimoto and S. Kuwabata, *Chem. Mater.*, 2023, **35**, 1094–1106.
36 O. Yarema, M. Yarema and V. Wood, *Chem. Mater.*, 2018, **30**, 1446–1461.
37 S. B. Zhang, S.-H. Wei, A. Zunger and H. Katayama-Yoshida, *Phys. Rev. B: Condens. Matter Mater. Phys.*, 1998, **57**, 9642–9656.
38 P. M. Allen and M. G. Bawendi, *J. Am. Chem. Soc.*, 2008, **130**, 9240–9241.
39 B. Chen, H. Zhong, W. Zhang, Z. A. Tan, Y. Li, C. Yu, T. Zhai, Y. Bando, S. Yang and B. Zou, *Adv. Funct. Mater.*, 2012, **22**, 2081–2088.
40 C.-M. Fan, M. D. Regulacio, C. Ye, S. H. Lim, Y. Zheng, Q.-H. Xu, A.-W. Xu and M.-Y. Han, *Chem. Commun.*, 2014, **50**, 7128–7131.
41 NIST X-ray Photoelectron Spectroscopy Database, NIST Standard Reference Database Number 20, National Institute of Standards and Technology, Gaithersburg MD, 20899, 2000, DOI: 10.18434/T4T88K.
42 M. Çadırcı, *J. Lumin.*, 2020, **228**, 117551.
43 P. Jing, J. Zheng, M. Ikezawa, X. Liu, S. Lv, X. Kong, J. Zhao and Y. Masumoto, *J. Phys. Chem. C*, 2009, **113**, 13545–13550.
44 A. Antipov, M. Bell, M. Yasar, V. Mitin, W. Scharmach, M. Swihart, A. Verevkin and A. Sergeev, *Nanoscale Res. Lett.*, 2011, **6**, 142.
45 J. W. de Wit, I. Zabala-Gutierrez, R. Marin, A. Zhakeyev, S. Melle, O. G. Calderon, J. Marques-Hueso, D. Jaque, J. Rubio-Retama and A. Meijerink, *J. Phys. Chem. Lett.*, 2024, **15**, 8420–8426.